Journal of Fluids and Structures 109 (2022) 103474

Contents lists available at ScienceDirect

Journal of Fluids and Structures

journal homepage: www.elsevier.com/locate/jfs

Parameter identification of wake-oscillator from wind tunnel data

François Rigo [a,b,c,*], Thomas Andrianne [a], Vincent Denoël [c]

[a] Wind Tunnel Lab, University of Liège, Belgium
[b] FRS-FNRS, National Fund for Scientific Research, Brussels, Belgium
[c] Structural & Stochastic Dynamics, University of Liège, Liège, Belgium

ARTICLE INFO

Article history:
Received 19 April 2021
Received in revised form 25 October 2021
Accepted 9 December 2021
Available online 24 January 2022

Keywords:
Vortex-induced vibrations
Wake-oscillator model
Perturbation methods
Synchronization
Wind tunnel experimental testing

ABSTRACT

This paper proposes a procedure for the parameter identification of Tamura's wake-oscillator model. A multiple timescale analysis of the dimensionless model shows that the response is governed by two dimensionless groups D_0 and D_1, highlighting the importance of the forcing terms in the two governing equations, the total (aerodynamic and structural) damping and the coefficient ε of the fluid Van der Pol oscillator. In particular, this approach provides a simple closed form expression for the steady state amplitude of the structural displacement, which is usually measured in wind tunnel experiments. The proposed method of identification consists in fitting the parameters of the model by adjusting the closed-form expression of the VIV curve on experimental points. It is developed into two variants: a least-square fitting and a fitting based on some simple geometrical indicators (height, width, asymmetry). The model is sufficiently versatile to estimate the maximum amplitude and lock-in range. Applications of VIV in air for different geometries and Scruton numbers show that the two variants give equivalent results thanks to the robustness of the method. The paper is first intended for experimenters looking for a simple robust procedure to identify the parameters of the wake-oscillator, which can then be used in a prediction phase. The derivation of the slow phase version of Tamura's model might also be appealing to better understand the main features of this model.

1. Introduction and motivation

Vortex-Induced Vibration (VIV) of bluff bodies subjected to smooth flows is a fluid–structure interaction. For medium to high Reynolds number (Lienhard, 1966), the flow behind bluff bodies is separated and vortices are ejected alternatively on both sides of the body. According to the Strouhal law, the vortex shedding frequency varies linearly with the incoming fluid velocity. Once this frequency matches the natural frequency of the structure left free to vibrate, the coupling between both degrees-of-freedom (structure and fluid) leads to the resonance of the structure. When the structure vibrates, the vortex shedding frequency does not follow the Strouhal law anymore and is locked to the natural frequency during a certain lock-in range of the fluid velocity (Païdoussis et al., 2010). The observable effect of VIV is a bell shape of the structural vibration amplitude versus fluid velocity, the resonance starting at the critical VIV velocity. There are many applications of VIV (in different fluids), which explains the amount of available VIV models (Gabbai and Benaroya, 2005). In wind engineering applications, flexible structures are subjected to various wind velocities during their lifetime. In

* Corresponding author at: Wind Tunnel Lab, University of Liège, Belgium.
E-mail address: francois.rigo@uliege.be (F. Rigo).

https://doi.org/10.1016/j.jfluidstructs.2021.103474
0889-9746/

these applications, a study on the potential presence of VIV has to be carried out in order to avoid undesirable vibrations, which can be very high (comparable to the cross-flow dimension of the structure) when the structure is light and slightly damped.

Vortex-Induced Vibration in air can be experimentally investigated in Wind Tunnel (WT) using rigid or flexible cylinders, instrumented with displacement transducer or laser for the structural motion and pressure sensor, cobra probe or hot wire for the fluid flow (wake) (Feng, 1968). For VIV experiments in one dimension, rigid cylinders with end-plates are used and two kinds of dynamic experiments can be made depending on cylinder supports: (i) forced (actuators) and (ii) free vibration (elastically-mounted). For a cylinder forced to move with an imposed motion, the amplitude is set between a fraction and the order of magnitude of the diameter and the forcing frequency is imposed around the static cylinder shedding frequency. When the amplitude and frequency are changed, it is possible to observes changes in the flow pattern (2S and 2P modes) (Williamson and Roshko, 1988). For a forcing frequency that would be observed with a cylinder at rest, there is no change in pattern but the shedding frequency does not follow anymore the Strouhal relation and is equal to the forcing frequency (wake capture). In free vibration, the elastically mounted cylinder is free to move and the motion is a result of its interaction with the wake. The cylinder dynamics depends on the mass and damping ratios, wind velocity, Reynolds number, natural frequency and cross section geometry. The VIV corresponds to the frequency matching between the shedding and natural frequency. This type of vibration is easy to implement in WT and the purpose is to measure the structural displacement as a function of the wind velocity. Some experimental studies also focus on 3D effects (Brika and Laneville, 1993; Gabbai and Benaroya, 2005) but they are not discussed here since the paper is based on two degrees-of-freedom models.

Different models have been proposed to represent this phenomenon. They are all based on an equation for the structural motion, complemented with some terms or equation(s) to take into account the interaction of the fluid with the structure. According to Païdoussis (Païdoussis et al., 2010), two-dimensional models are classified into three families. Forced system models (type A) use the fluid as an external excitation through a lift force (from static cylinder experiments). This classical linear vibration problem is able to predict amplitude at large Skop–Griffin (SG) numbers and the lock-in is not captured. Fluid elastic models (type B) use a feedback to make the lift force dependent of the motion (amplitude, velocity, acceleration or a combination). The modified forcing model of Blevins (1990) uses data of an oscillating cylinder in forced motion to obtain the variation of lift with amplitude, allowing to capture the self-limiting features of the phenomenon (Larsen, 1995; Marra et al., 2011; Lupi et al., 2018). Other advanced forcing models use the concept of phased lift coefficients. Time domain fluidelastic models of Chen (Chen et al., 1995) or Simiu and Scanlan (Simiu and Scanlan, 1996) have an explicit use of the time dependency by using added mass, damping, stiffness or a nonlinear term to account for amplitude effect in the lift force expression. Types A and B are nevertheless limited to harmonic motions (difficult to generalize to more complex motions and do not physically interpret the wake as an additional degree-of-freedom having its own dynamics. In type C, wake-oscillator models use the principle that "fluid force is the result of the wake dynamics, itself influenced by the cylinder motion" (Païdoussis et al., 2010). This leads to a coupled differential system with two variables : the structure and the wake. The fluid has thus its own dynamics, with a limit cycle which makes it susceptible to synchronize. Van der Pol or Rayleigh oscillators are known to present these features and have been used in various models (Hartlen and Currie, 1970; Tamura, 1981; Facchinetti et al., 2004; Krenk and Nielsen, 1999; Farshidianfar and Zanganeh, 2010). Models differ on the fluid variable and the type of forcing of the fluid equation. Facchinetti (Facchinetti et al., 2004) used a reduced lift and a forcing term proportional to the structural acceleration. This paper focuses on the wake-oscillator model proposed by Tamura (1981). It relies on Birkhoff's concept about the oscillating wake. The forcing of the fluid equation depends on a combination of structural acceleration and velocity. Despite the number of models, their practical use is often difficult because of the need for simple methods to identify model parameters, which is the main motivation of the present study. To the authors' knowledge, there is currently no general identification method for wake-oscillator models (type C) from free vibration tests. In this paper, we describe a novel method to identify the parameters of Tamura's model on the basis of typically available experimental observations. The potential candidates are: (i) the maximum displacement amplitude, (ii) the size of the lock-in region and (iii) sometimes the wake dynamic (phase) to predict entirely the instability. Nevertheless, the phase is difficult to measure experimentally so that the present identification procedure is solely based on the displacement and lockin range (Varty and Currie, 1984; Labraga et al., 2007).

This phase angle is actually varying slowly with time; it plays a major role in synchronization problems (Denoël, 2020; Pikovsky et al., 2003). In the present study, it allows to understand the coupled dynamics between the structural motion and the oscillating wake. Nevertheless, the experimental measurement of the phase is difficult because it depends on the wake degree-of-freedom, which can be measured using the separation points but is practically complex to capture (Varty and Currie, 1984).

In this study, we avoid solving the fast dynamics of the problem but only resolve its slow dynamics using the phase, which results in a simple algebraic equation. The structure and wake response envelopes are then derived from the slow phase. This asymptotic analysis at first order allows to express the response using only three dimensionless groups and two other parameters.

Because it is based on the fitting of a simple analytical expression, the proposed model simplifies the identification of the parameters of Tamura's model and makes it more robust. Indeed, a lot of parameters have to be measured or empirically derived, to use the model.

The paper is organized as follows. In Section 2, Tamura's model is introduced, with its main parameters, in a dimensionless version. The averaged version of the system is derived, leading to a slow phase model. The effect of

dimensionless groups on the VIV response is analysed through model features in Section 3, with a focus on ranges of numerical values of typical applications. The parameter identification methodology is then presented in Section 4. It shows the possibility to obtain model parameters in two cases : (i) a least-square fitting for detailed experimental VIV curve and (ii) a fitting based on global geometric indicators of the VIV curve. Applications are shown in Section 6 to get typical values of model parameters and compare the two variants of the proposed method. A discussion on physical parameters and their use in a prediction procedure is finally presented in Section 7.

Nomenclature

Wake-oscillator parameters	
t	Time (s)
$(\cdot)' = d(\cdot)/d\tau$	Derivative with respect to τ
$\tau = 2\pi f_0 t = \omega_0 t$	Dimensionless time
μ	Air dynamic viscosity (kg/m/s)
ρ	Air density (kg/m^3)
y	Transverse displacement of the oscillating cylinder (m)
$Y = y/D$	Dimensionless transverse displacement of the cylinder
D	Diameter, cross-flow dimension (m)
α	Angular position of the wake (rad)
f_0	Natural frequency of transverse vibration (Hz)
f_{vs}	Vortex shedding frequency (Hz)
m	Mass per unit length of the oscillating body (kg/m)
$m_r = \rho\pi D^2/4m$	Fluid/Structure mass ratio
U	Wind velocity (m/s)
$U_{cr} = f_0 D/St$	Critical VIV velocity (m/s)
C_D	Drag force coefficient
C_{L0}	Amplitude of oscillation of the lift coefficient
$Re = \rho UD/\mu$	Reynolds number
$Sc = \pi^2\xi/m_r$	Scruton number (Scruton, 1981)
$SG = 4\pi^2 St^2 Sc$	Skop–Griffin number
$St = f_0 D/U$	Strouhal number
f	Lift coefficient per unit rotation of the equivalent wake coordinate (Magnus effect)
$L^*, \lambda = 1/(0.5 + L^*)$	Dimensionless half length of wake-oscillator
$\varepsilon = f\sqrt{2}\pi^2 L^*$	Coefficient on nonlinear damping term in the wake equation (Van der Pol coefficient)

Dimensionless model parameters	
ξ_s, ξ_a	Structural and aerodynamic damping ratios
$\xi = \xi_s + \xi_a$	Total damping ratio
$\xi_0 = \xi/\varepsilon$	Reduced damping ratio
$T = \varepsilon\tau$	Slow time
$\Omega = U/U_{cr}$	Velocity ratio, mistuning, bifurcation parameter
$\delta = (\Omega - 1)/\xi$	Centred and scaled mistuning, bifurcation parameter
M_0	Dimensionless fluid/structure mass ratio
D_0, D_1	Dimensionless groups characterizing the response of the wake oscillator model
$R_y(T)$	Envelope of the structural response $\tilde{Y} = Y/\varepsilon$
$R_\alpha(T)$	Envelope of the wake variable $\tilde{\alpha} = \alpha/(C_{L0}/2f)$
$\psi(T)$	Slow phase between $\tilde{Y}$ and $\tilde{\alpha}$

2. The wake-oscillator model

2.1. Dimensionless governing equations

The present study is based on the wake-oscillator model from Tamura (1981). This model is a generalization of other wake-oscillator models such as Facchinetti et al. (2004) or Hartlen and Currie (1970). It is based on physical and empirical interpretation and is expressed using a system of two degree-of-freedom differential equations. The dimensionless version of Tamura model reads :

$$Y'' + \left(2\xi_s + m_r(f + C_D)\frac{\Omega}{2\pi St}\right)Y' + Y = -\frac{f m_r \Omega^2}{(2\pi St)^2}\alpha \tag{1}$$

$$\alpha'' + \varepsilon\Omega\left(\frac{4f^2}{C_{L0}^2}\alpha^2 - 1\right)\alpha' + \Omega^2\alpha = -\lambda Y'' - \Omega 2\pi St Y' \tag{2}$$

where $Y = y/D$ is the dimensionless cross-flow structural motion, D the cylinder diameter (or characteristic cross-flow dimension), α the position of the wake lamina due to vortex shedding. $(\cdot)'$ denotes the derivative with respect to $\tau = 2\pi f_0 t = \omega_0 t$, where $\omega_0 = \sqrt{k_s/m}$ with k_s the stiffness of the structure and m the mass of the oscillating body ($m = m_s + m_f$ is the sum of the structural mass m_s and equivalent mass of displaced fluid m_f (negligible in wind engineering applications). The structural damping ratio is $\xi_s = c_s/(2\sqrt{k_s m})$ where c_s is the viscosity of the structure. The velocity ratio is $\Omega = U/U_{cr}$ where U is the fluid velocity and $U_{cr} = f_0 D/St$ is the critical VIV velocity. C_D and C_{L0} are the stationary drag coefficient and the magnitude of the lift coefficient fluctuations on the fixed body, St the Strouhal number. Force measurement in static cylinder experiments allows to obtain C_D and C_{L0}. Wake analysis in static cylinder experiments gives St. Some parameters have to be adjusted and are obtained from an empirical procedure: f is the lift coefficient per unit rotation of the equivalent wake coordinate (linked to Magnus effect), λ is related to the length of the oscillating wake and ε is the damping ratio of the wake-oscillator. This dimensionless parameter describes the memory in the wake equation and is linked to the magnitude of the nonlinearity in the Van der Pol equation for the wake, therefore to the strength of the limit cycle. The present study is a generalization of a similar study of Facchinetti model, for which an asymptotic analysis has already been developed, showing that the timescales can be advantageously separated; more details on the procedure can be found in Denoël (2020).

2.2. Asymptotic analysis

Instead of solving this two degree-of-freedom multiple scale problem (1)–(2), a perturbation method is used (Hinch, 1991). This perturbation analysis requires the identification of *small* numbers in the physical quantities (Mannini, 2020). The small parameter ε in the wake equation plays a crucial role in the dynamics by controlling the nonlinearity of the Van der Pol wake equation and is used to derive an asymptotic solution of this problem. Experimentally, the dimensionless transverse amplitude Y is limited to *small* oscillations, typically 0.1–0.3 (2S vortex shedding regime (Williamson and Roshko, 1988)). This motivates to express $Y = \varepsilon\tilde{Y}$, where $\varepsilon \ll 1$ and $\tilde{Y} \sim 1$. The wake coordinate α is expressed as $\tilde{\alpha} = \alpha/\alpha^*$ with $\alpha^* = C_{L0}/2f$ to simplify the nonlinear term in Eq. (2). The distinguished limit is fulfilled as long as the mass ratio m_r is of the order ε^2. The mass ratio is then written as $m_r = \varepsilon^2 m_{r,0}$ with $m_{r,0} \sim 1$. Indeed, the fluid to solid mass ratio in wind engineering applications (light structures submitted to wind) is typically very small ($m_r \sim 10^{-4} - 10^{-3}$). The total damping ξ is the sum of the structural (ξ_s) and aerodynamic damping ($\xi_a = m_r(f + C_D)\Omega/4\pi St$). For steel structures in wind engineering applications, a low damping is considered (typically $\xi \sim 0.1 - 0.3\%$). For this reason, we suppose $\xi = \varepsilon\xi_0$. Another choice could be $\xi = \varepsilon^2\xi_0$, as proposed by Denoël (2020) who showed that it will lead to the same results after mathematical developments as soon as ξ is as large as ε.

The system is solved to obtain the VIV response, for wind velocities in the lock-in range. This interval corresponds to wind velocities close to the critical one, suggesting a small mistuning, i.e. $\Omega \sim 1$. In forced vibration, Ω is driven by ε whilst in free vibration (present case), it is more appropriate to rescale the mistuning as $\Omega = 1 + \xi\delta$, see (Denoël, 2020), it is justified by results below. Because ξ is a small parameter, δ is the mistuning parameter of order 1. The short and compact version of the governing equations is:

$$\tilde{Y}'' + 2\xi\tilde{Y}' + \tilde{Y} = 2\varepsilon M_0\tilde{\alpha} \tag{3}$$

$$\tilde{\alpha}'' + \varepsilon\Omega\left(\tilde{\alpha}^2 - 1\right)\tilde{\alpha}' + \Omega^2\tilde{\alpha} = 2\varepsilon(A_0\tilde{Y}'' + A_1\Omega\tilde{Y}') \tag{4}$$

where

$$M_0 = -\frac{m_r C_{L0}}{16\pi^2\varepsilon^2}\left(\frac{\Omega}{St}\right)^2 = -\frac{C_{L0}\xi\Omega^2\pi}{2\varepsilon^2 SG}, \qquad A_0 = -\frac{\lambda f}{C_{L0}}, \qquad A_1 = -\frac{2\pi Stf}{C_{L0}}. \tag{5}$$

These equations are now expressed using two variables of order 1 ($\tilde{Y}$ and $\tilde{\alpha}$) and three dimensionless groups (A_0, A_1 and M_0). By using a multiple scale approach (averaging), a solution is sought with two time scales $t_1 = \tau$ (fast) and

$t_2 = T = \varepsilon\tau$ (slow). An Ansatz is used for both variables: $\tilde{Y} = \tilde{Y}_0 + \varepsilon\tilde{Y}_1 + \mathcal{O}(\varepsilon^2)$ and $\tilde{\alpha} = \tilde{\alpha}_0 + \varepsilon\tilde{\alpha}_1 + \mathcal{O}(\varepsilon^2)$ and its substitution into Eq. (3)–(4) gives, at leading order:

$$\tilde{Y}_0 = R_y(T)\cos(\tau + \phi(T)) \tag{6}$$

$$\tilde{\alpha}_0 = R_\alpha(T)\cos(\tau + \phi(T) + \psi(T)). \tag{7}$$

For both degrees of freedom, the solution at leading order is a fast oscillation modulated by a slow envelope and featuring a slow phase $\psi(T)$. Solving the system for the envelopes R_y, R_α and the phase ψ, the secularity conditions at the next order allow to obtain three first order differential equations (details in Appendix A.1). In steady-state condition, all lefthand sides vanish and solving for the steady phase gives:

$$\cot^3\psi + \delta\cot^2\psi + (1 + D_0)\cot\psi + \delta - D_1 = 0 \tag{8}$$

$$R_y = 2\frac{M_0}{\xi_0}\sin\psi\sqrt{1 + 2\xi_0 D_0\sin^2\psi + \xi_0 D_1\sin 2\psi} \tag{9}$$

$$R_\alpha = 2\sqrt{1 + 2\xi_0 D_0\sin^2\psi + \xi_0 D_1\sin 2\psi} \tag{10}$$

where

$$D_0 = \frac{A_0 M_0}{\xi_0^2} = \frac{\pi\lambda f\Omega^2}{2\xi SG}, \qquad D_1 = \frac{A_1 M_0}{\xi_0^2} = \frac{\pi^2 Stf\Omega^2}{\xi SG} \tag{11}$$

Notice that a scaling of Ω with ε would have introduced $\delta\varepsilon/\xi$ instead of δ in Eq. (8). This justifies the choice of $\Omega = 1 + \xi\delta$ in free vibration. D_0 and D_1 are the driving parameters of VIV response predicted by the Tamura's model. These dimensionless groups are always positive. The dimensionless group D_1 leads to asymmetric VIV curves. It is equal to zero in the Facchinetti's model (Denoël, 2020). The mistuning δ is the driving parameter in Eq. (8)–(10). The phase ψ the main unique variable from which the structural envelope R_y is deduced. Indeed, knowing physical parameters in D_0 and D_1, the phase can be directly computed as a function of δ by solving Eq. (8). Then, the envelope of the displacement is obtained from Eq. (9) The main result of this method is the transition from a differential system to simple algebraic equations (Eq. (8)–(9)).

3. Effect of dimensionless groups

The perturbation method presented in Section 2 showed the key role of the phase ψ in the results. Eq. (8) is solved in Fig. 1 to obtain the cotangent of the phase, $\cot\psi$, as a function of the mistuning δ for different values of the constants D_0 and D_1. When $D_0 = D_1 = 0$, there is no coupling term and it corresponds to type A (forced models). The cases $D_0 = 0$ or $D_1 = 0$ are shown to make the link with other kinds of VIV models that use only one coupling term in the fluid equation (only the acceleration ($D_1 = 0$) for Facchinetti model (Facchinetti et al., 2004; Denoël, 2020) or the velocity ($D_0 = 0$) for Hartlen–Currie model (Hartlen and Currie, 1970)). Tamura's wake-oscillator model is thus a generalized model that combines the features of Facchinetti and Hartlen–Currie models. When $\cot\psi = 0$, the phase $\psi = \pi/2$ and the fluid force (right hand side of the structural equation (3)) is in phase with the structural velocity, leading to a maximum energy transfer between the flow and the structural motion. This results possibly in large transverse vibration if $SG \ll 1$ (critical velocity $\Omega = 1$ when $\delta = 0$). Note that when $\delta = 0$, $\cot\psi \neq 0$ if $D_1 > 0$. Instead the maximum energy transfer corresponding to $\cot\psi = 0$ occurs for $\delta > 0$ or $\Omega \geq 1$, i.e. above the frequency matching as observed experimentally. Also, by inspecting Eq. (8), $\cot\psi = 0$ leads to $\delta = D_1$ (independently of D_0), as illustrated in Fig. 1 by symbols $\circ$ ($D_1 = 0$) and $\diamond$ ($\delta = D_1 = 12$). For $\cot\psi$ *close* to 0, the phase is still close to $\pi/2$ and vibration amplitudes can be still large, in the lock-in range. It is observed from Fig. 1 that $D_1 = 0$ (black lines) gives a symmetric lock-in. In that case, a critical value of D_0 is 8 (from Cardano formula) with a vertical tangent point near $\delta = -5$ in Eq. (8). There is a hysteresis (three real roots in Eq. (8)) in $\cot\psi$ for $D_0 > 8$ meaning that: (i) two stable branches are present and can be accessed depending on an increasing or decreasing δ and (ii) one unstable branch is present between the two others. The effect of D_1 is an asymmetrisation of the response, that grows with D_1. For a sufficiently high D_1, the hysteresis for $\delta < 0$ created by $D_0 > 8$ can disappear, e.g. $D_0 = 16$ and $D_1 = 12$ in Fig. 1.

Fig. 2 shows the envelope of the transverse displacement *Ry* as a function of the mistuning δ for $D_0 = 1$ and $D_1 = 8$. These values were chosen to have only one hysteresis in the right part of the VIV curve and a case study for comparison with simulations. Black lines are analytical results obtained by substituting $\cot\psi$ in Eq. (9). The blue and red lines are the transient numerical solutions of the full model by slowly ramping up or down the mistuning. The blue dots and red crosses are numerical results from the full model (Eq. (1)–(2) or (3)–(4), with parameters given in the caption) representing the steady state solution, using initial conditions chosen as the steady state solution of the previous one. The mistuning parameter δ is ramped up or down.

The introduction of dimensionless groups (D_0, D_1) allow to study characteristic of the different VIV responses. Systems with different physical parameters (such as *SG* and C_L) but with the same dimensionless groups D_0, D_1 lead to the same type of response.

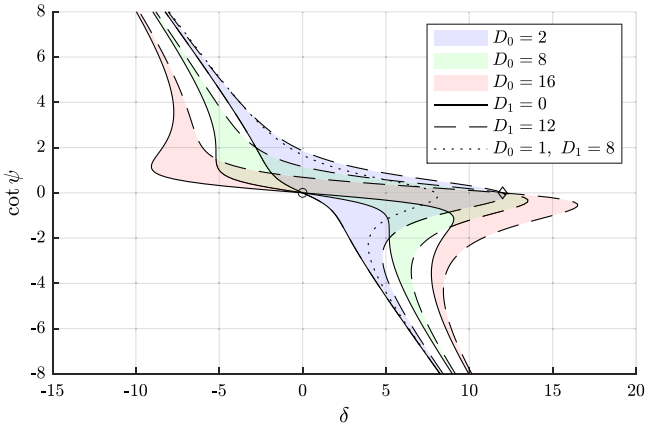

Fig. 1. Phase vs mistuning: effect of D_0 and D_1 on the solution of Eq. (8), $\cot\psi = 0$ at $\circ$ ($\delta = 0, D_1 = 0$) and at $\diamond$ ($\delta = D_1 = 12$). (For interpretation of the references to colour in this figure legend, the reader is referred to the web version of this article.)

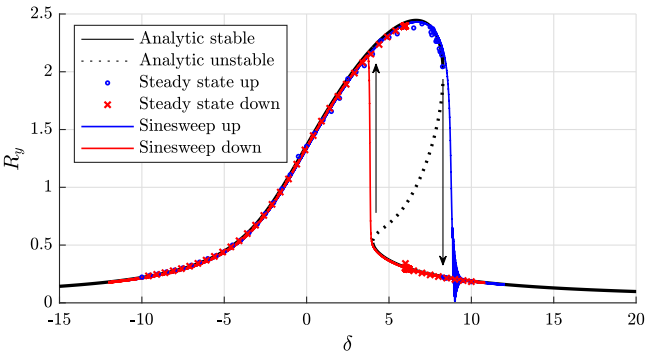

Fig. 2. Amplitude vs mistuning: analytic (in black, with $D_0 = 1$, $D_1 = 8$) and numerical results (in red, blue, with $\xi = 0.005, \varepsilon = 0.05, M_0 = 0.1, A_0 = 0.1, A_1 = 0.8$).

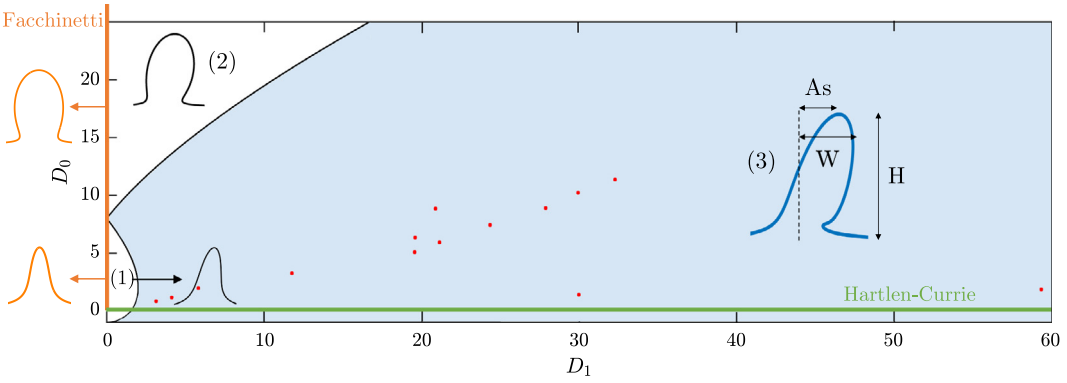

Fig. 3. Features of the model: VIV curve shape and hysteresis as a function of D_0 and D_1: (1) no hysteresis, (2) hysteresis on both sides and (3) hysteresis on the right. The orange line shows symmetric VIV curves ($D_1 = 0$) of Facchinetti model (Facchinetti et al., 2004) and the green one shows the case $D_0 = 0$ of Hartlen–Currie model (Hartlen and Currie, 1970). Red dots correspond to experimental results of Section 6. (For interpretation of the references to colour in this figure legend, the reader is referred to the web version of this article.)

Fig. 3 presents the features of the model: the shape and hysteresis behaviour of R_y depending on D_0, D_1. Only positive values of D_0, D_1 are represented because the parameters in their definition of Eq. (11), associated to wind engineering applications, always lead to positive values.

On the vertical axis, VIV curves are symmetric and correspond to the particular case of Facchinetti model ($D_1 = 0$). For D_0 between 0 and 8, there is no hysteresis (zone (1)). For $D_0 > 8$, hysteresis are present on both sides (zone

(2)). When D_1 increases, the curve is asymmetric to the right with hysteresis on both sides. When D_1 increases (and $D_0 < 8$), the curve is asymmetric to the right (blue region (3)) and becomes a right hysteresis for D_1 greater than the boundary between zones (1) and (3). For D_1 greater than the black line boundary between zone (2) and (3), the left hysteresis disappears, leading to the blue region. This kind of hysteresis behaviour is well known in nonlinear control theories and a link with the Winged Cusp unfolding (Golubitsky et al., 1989; Glendinning, 1994) can be made with $x \to \cot\psi,\ \lambda^2 \to \delta,\ \beta \to 1 + D_0,\ \gamma \to -D_1$.

Experimentally, most of observed VIV curves correspond to the case where a hysteresis is present on the right, i.e. in the blue zone (3) of Fig. 3. Red dots in this Figure correspond to examples of value (D_0, D_1) of WT and wind engineering (full scale) applications. The VIV curve can be characterized by three geometric indicators as illustrated in Fig. 3. A link between these indicators and groups D_0, D_1 is made :

- H: maximum amplitude of the curve,
- W: width of the lock-in range,
- As: asymmetry when $D_1 > 0$ (location of this maximum response).

The present identification method is based on an asymptotic analysis highlighting that dimensionless groups D_0, D_1 drive the VIV.

4. Identification method

The proposed procedure to identify the wake-oscillator parameters from free vibration WT data is detailed in this section and its two variants are illustrated Fig. 4. From experimental data, dimensionless groups can be identified by two different techniques. Then, by returning to their definition, the physical parameters of the wake-oscillator model are derived and can be further used in a prediction phase.

The two proposed options depends on the VIV curve discretization : (i) a least-square fitting procedure for a detailed VIV curve and (ii) the use of some geometric indicators when only the envelope is measured. Since the proposed fitting involves 3 parameters, it is recommended to use at least 10 points for the first option. The second option was imagined to cover cases with a scarcer density of data points across the VIV curve. The applications will show that both methods give equivalent and accurate identification results. The use of three geometric indicators can thus be sufficient and there is no need to measure a detailed VIV curve, as long as H, W and As are accurately captured. In this sense, the perturbation method developed in Section 2 is robust.

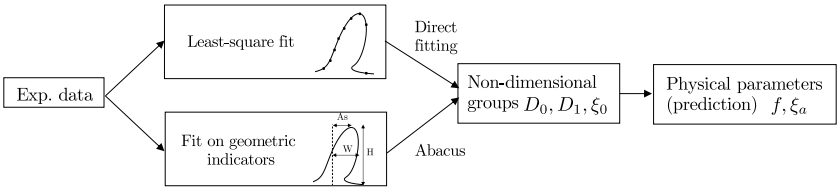

Fig. 4. Parameter identification procedure.

4.1. Option 1 : Least-square fitting

The fitting procedure for a given data set consists in adjusting the model parameters $\boldsymbol{\pi} = \{D_0, D_1, \xi_0\}$ in order to minimize the residuals between the VIV curve R_y derived in the asymptotic analysis and a non-parametric estimate Y_i^* of the experimental VIV curve measured for n_p values of δ. Formally, parameters and dimensionless groups are obtained by solving the following minimization problem,

$$\hat{\boldsymbol{\pi}} = \arg\min_{\boldsymbol{\pi}} \sum_{i}^{n_p} \left(R_y(\psi(\delta_i); \boldsymbol{\pi}) - Y_i^*\right)^2 \tag{12}$$

where $R_y(\psi(\delta_i); \boldsymbol{\pi})$ is given by Eq. (9) and $\psi(\delta_i)$ by Eq. (8). $Y_i^* = \sqrt{2}y_i'/D$ with y_i' the root mean square of the displacement measured for mistuning δ_i. The fitting procedure is performed with a nonlinear least-square algorithm as $R_y(\psi)$ and $\psi(\delta)$ are nonlinear in terms of δ.

As introduced in Section 3, typical VIV curve are characterized by a clutch shape shifted to the right with respect to $\Omega = 1$. Indeed, VIV starts at the critical velocity and lasts over a certain velocity range (lock-in). During the asymptotic analysis of Section 2, ξ_0 was assumed of order one at most and consequently in the range [0, 1]. As explained in Section 3, D_0 and D_1 are always positive. In a bounded and known parameters space, inspired by the physics, the search of an optimum of the problem, represented by its objective function $F(\boldsymbol{\pi}) = \sum_i \left(R_y(\psi(\delta_i); \boldsymbol{\pi}) - Y_i^*\right)^2$, is facilitated.

Numerically, a Levenberg–Marquardt algorithm (implemented by default in Matlab (2019)) has been used and a sensitivity analysis to initial guesses has been performed to assess the robustness of the procedure. The complete numerical implementation of such a minimization procedure is not discussed here as many optimization packages are available in shared libraries.

4.2. Option 2 : Geometric indicators

The identification can also be performed on the basis of simple geometric indicators. This section presents the analytical link between the model solution (Eqs. (8)–(9)) and these indicators. In short, the direct analysis of the average model allows to determine the 3 geometrical indicators W, H, As as a function of D_0, D_1 and ξ_0. The basis idea in the second option is to derive these expressions and to invert them in order to express D_0, D_1, ξ_0 as a function of measured geometric indicators.

For the sake of simplicity, the amplitude and phase equations (Eq. (8)–(9)) are rewritten using $c = \cot\psi$,

$$c^3 + \delta c^2 + (1 + D_0)c + \delta - D_1 = 0 \Leftrightarrow \delta = \frac{D_1 - c^3 - (1 + D_0)c}{c^2 + 1} \tag{13}$$

$$R_y = 2\frac{M_0}{\xi_0(c^2+1)}\sqrt{c^2 + 1 + 2\xi_0 D_0 + 2c\xi_0 D_1}. \tag{14}$$

Label A is the maximum amplitude $\mathrm{H} = R_{y,A}$. It is obtained by differentiating R_y with respect to δ (and equivalently to $c = \cot\psi$ as it can be seen in Fig. 5c).

$$\frac{dR_y}{d\delta} = 0 \;\Leftrightarrow\; \frac{dR_y}{dc} = 0 \overset{\text{Appendix A.1}}{\Longleftrightarrow} c_A^3 + 3\xi_0 D_1 c_A^2 + (1 + 4\xi_0 D_0)c_A - \xi_0 D_1 = 0 \tag{15}$$

Solving Eq. (15) for c_A and injecting in Eq. (13) and (14) gives the analytical expression for maximum amplitude H and δ_A respectively.

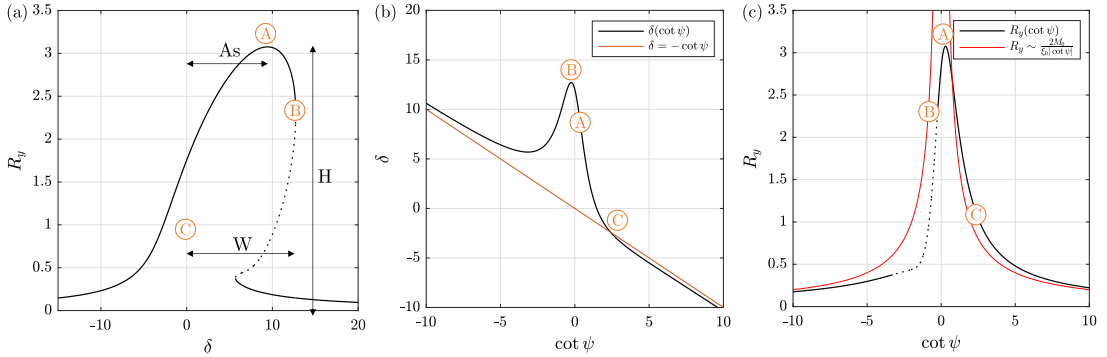

Fig. 5. Model results for $D_0 = 5$, $D_1 = 12$ with labels (A, B, C) : (a) Amplitude vs mistuning with geometric indicators (H, W, As), (b) Phase vs mistuning, (c) Amplitude vs phase.

Label B corresponds to a conventional end of the lock-in region and mathematically to a local maximum in the $\delta - c$ graph (Fig. 5(b)), such that

$$\frac{d\delta}{dc} = 0 \Leftrightarrow -c_B^4 + c_B^2(D_0 - 2) - 2D_1 c_B - (1 + D_0) = 0 \tag{16}$$

This equation has 4 roots and at least 2 of them are real given the range of D_0 and D_1 : in Fig. 5(b), they correspond to label B (extremum of the VIV curve) and the local minimum on its left (local extremity of the lower hysteresis branch). From c_B, the corresponding δ_B is obtained with Eq. (13). This is only valid in the zone where there is some hysteresis on the right (zone (3) in Fig. 3).

Label C is associated to the onset of VIV and the simplest criterion for it is to take $\delta_C = 0$. Other criteria were investigated but appeared arbitrary compared to the systematic nature of $\delta = 0$ and its ease of use for Wind Tunnel applications. The width of the VIV curve is then defined as a function of (D_0, D_1) using labels B and C.

Similarly, the asymmetry is defined with labels A and C. This direct analysis allows to compute the width, asymmetry and height as a function of dimensionless groups D_0, D_1 and ξ_0:

$$\mathrm{W} = \delta_B - \delta_C, \qquad \mathrm{As} = \delta_A - \delta_C, \qquad \mathrm{H} = R_{y,A}. \tag{17}$$

It is unfortunately not possible to express D_0, D_1 and ξ_0 as a function of W, H and As, by means of a simple closed-form expression. Instead, the analysis of the expressions for W, H and As allows one to simplify the solution of this inversion (i.e. identification). In particular, from Eq. (14), in the centre of the lock-in range, $c \ll 1$, thus $R_y \sim \xi_0^{-1}\sqrt{1 + 2\xi_0 D_0}$. For $D_0 \gg \xi_0^{-1}$ and by noting that $D_0 \sim \xi_0^{-2}$ (from the definition of D_0 in Eq. (11)), we have $R_y \sim \xi_0^{-3/2}$ if $2\xi_0 D_0 \gg 1$, which is the case as $\xi_0 \in [0, 1]$ and $D_0 > 1$ usually (this will be illustrated in Section 6). A map of $\mathrm{H}\xi_0^{3/2}$ can then be computed depending only on D_0 and D_1. In case $D_0 \gg \xi_0^{-1}$ is not verified but if $2\xi_0 D_0 \ll 1$, the approximation to build the map $\mathrm{H}\xi_0^{3/2}$ can be used. Nevertheless, to be more accurate, the system of three Eqs. (13)–(15)–(16) can be solved but is more cumbersome than this semi-graphical method with $\mathrm{H}\xi_0^{3/2}$.

From Eq. (15), the solution c_A depends on $\xi_0 D_0$ and $\xi_0 D_1$ as detailed in Appendix. Nevertheless, the corresponding c_A is very small near the maximum R_y and from Eq. (13), the corresponding δ mainly depends on D_1. From Eq. (16), independent on ξ_0, the width W depends on D_0 and D_1. Based on these observations, a two-way relation can however be derived by creating maps of H, W and As for different (D_0, D_1) (Fig. 6).

From experimental measurements of a VIV curve, this procedure allows to deduce the effect of D_0 and D_1 on H, W and As: D_0 has more influence on H, D_1 on As and both equivalently on W. The parameter identification procedure of Fig. 6 is performed in 4 steps:

i determine W, H, As from measured VIV response
ii pick the iso contours corresponding to the observed W and asymmetry As
iii identify the intersection between the W and As isocontours on $H\xi_0^{3/2}$ map to deduce its value and D_0, D_1.
iv compute ξ_0 knowing H from experimental data.

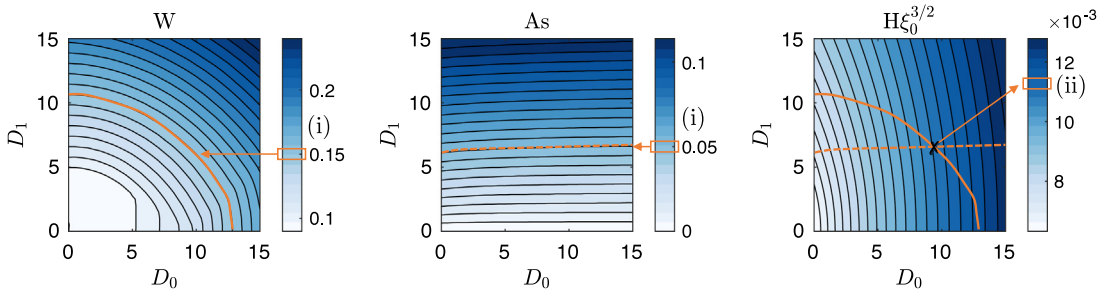

Fig. 6. Influence of D_0 and D_1 on geometric indicators H, W and As and identification procedure of ξ_0.

5. Numerical validation

The sensitivity of parameters in the proposed procedure has been performed by analysing the objective function $F(\boldsymbol{\pi}) = \sum_i \left(R_y(\psi(\delta_i); \boldsymbol{\pi}) - Y_i^*\right)^2$ in the neighbourhood of the optimal found parameters using experimental data Y_i^* presented in Section 6 (the 4:1 rectangle with $Sc = 1.9$). The parameters space is multidimensional and Fig. 7 shows cuts of this objective function in different planes: (D_0, ξ_0), (D_1, M_0) and (D_0, D_1). Fig. 7 shows a smoothly varying $F(D_0, \xi_0)$ around $(10, 0.12)$ (first line in Table 2). The identified minimum of the objective function over a wide range of parameters appears to be a global one, which confirms the robustness of the method. The same conclusion can be drawn from the shape of $F(D_1, M_0)$: the function is regular and smooth with homogeneous gradients towards the global minimum of F. In the (D_0, D_1) plane, gradient in D_1 direction is higher than the one along D_0. Small variations of D_0 have less influence on the objective function value than D_1 but the optimum is well identified.

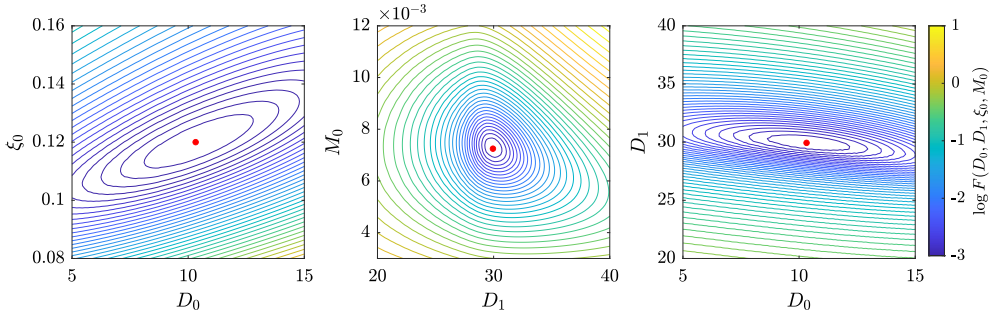

Fig. 7. Contour plots of the objective function $F(\boldsymbol{\pi})$ in log-scale, found optimum in red. (For interpretation of the references to colour in this figure legend, the reader is referred to the web version of this article.)

A validation study has been performed by simulating the response for fixed (known) model parameters $\boldsymbol{\pi} = (D_0, D_1, \xi_0)$. One parameter at a time has been modified in a wide interval of values and compared with the estimated value from the proposed procedure. Fig. 8 shows the comparison between given model parameters $\boldsymbol{\pi}$ and the estimated ones $\hat{\boldsymbol{\pi}}$ (values in blue dots with the one-to-one red line). The correspondence between them is high in a wide range of parameters, which again validates the proposed procedure.

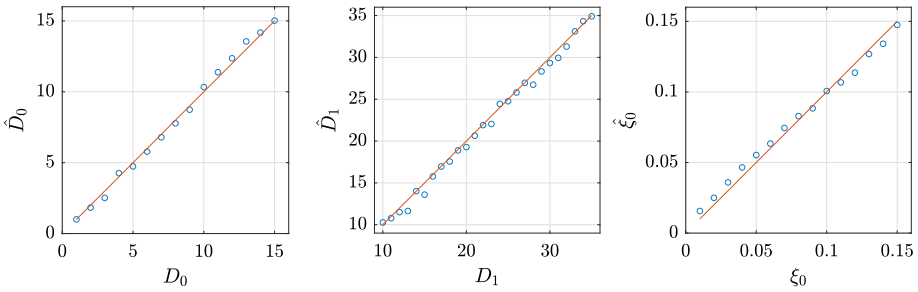

Fig. 8. Comparison of given parameters $\boldsymbol{\pi}$ for simulated response to estimated ones $\hat{\boldsymbol{\pi}} = (\hat{D}_0, \hat{D}_1, \hat{\xi}_0)$.

6. Applications

The identification methodology is applied to several wind tunnel data sets obtained from spring mounted rigid models. Several geometries (circular, square, rectangular) and Scruton number are considered in a Reynolds number range around 10^4. Literature (Marra et al., 2015; Wawzonek, 1979; Amandolèse and Hémon, 2010; Feng, 1968) results and present dedicated wind tunnel experiments (at University of Liège, see Appendix A.2) are considered. The main parameters of the selected experimental data are gathered in Table 1.

Table 1
VIV wind tunnel setup parameters.

Section shape	Reference	Re_{cr}	St	ξ_s [%]	m_r	Sc	f_0 [Hz]	D [m]
4:1 Rectangle	Marra (Marra et al., 2015)	$2 \cdot 10^4$	0.137	0.058–2.34	0.0038	1.9–78.1	7.97	0.075
Square	Present	$2 \cdot 10^4$	0.12	0.06	0.0016	3.9	8.06	0.05
"	Wawzonek (1979)	$2.2 \cdot 10^4$	0.12	0.08	0.0013	7.5	5.22	0.051
"	Amandolèse (Amandolèse and Hémon, 2010)	$8 \cdot 10^3$	0.12	0.09	0.0011	9.4	15.2	0.02
Circular	Present	$2 \cdot 10^4$	0.2	0.11–0.3	0.0038	3.7–8.9	7.08	0.1
"	Feng (1968)	$2.5 \cdot 10^4$	0.2	0.1–0.13	0.004	3.1–4	9.04	0.076

Fig. 9 presents the experimental VIV curve from the literature for the 4:1 rectangle, square and circular sections for different Sc. The main results of the parameter identification procedure are graphically represented by (i) the least-square model fitting (option 1, left column) and (ii) geometric indicators (option 2, right column). The associated dimensionless groups are detailed in Table 2. The fitted analytic VIV curves are represented in a ramping up way (increasing velocity). The apparent discontinuity is due to the presence of a hysteresis on the right in the model, with an unstable branch in-between that is usually not observed experimentally.

Regardless of Sc and sections shapes, it is noted that VIV starts around $\Omega = 0.95$. There is a very good agreement of model fitting with 4:1 rectangle and square. Option 2 gives also good results considering the lock-in width and maximal amplitude prediction. However, the whole VIV curve deviates slightly from experimental data. Indeed, in option 2, the focus is set to global indicators, but no weight is associated to every single point in the VIV curve.

Nevertheless, the curve obtained with option 2 matches the envelope of the experimental VIV curve but locally, the model estimate does not follow all experimental points. The fine discretization of experimental data for the 4:1 rectangle allows to compare precisely different Sc and fitting procedures. For low Sc, the VIV shape from the model accurately matches the experimental one. For the largest Sc (78.1), the experimental curve becomes nearly symmetric around $\Omega \sim 1.1$. The asymmetric lock-in is well captured by the model but the shape cannot have a symmetric bell shape about $\Omega \sim 1$, which explains the discrepancy with the WT data. For the square section, the characteristic shape of the model is able to capture accurately the WT data curve for all Sc presented.

For the circular cylinder of the present (ULiège) WT setup, it was possible to reproduce the lower (hysteresis) branch that Feng (Feng, 1968) obtained. Using a small wind velocity increment, the region where the amplitude increases to 0.35 was followed by a sudden drop to 0.2 and a slow decrease to the end of the lock-in at around $\Omega = 1.42$. Then, starting from a higher velocity and using a small decrement, the lower bell shape branch was obtained, without reaching the maximum amplitude of 0.35. For this lowest Sc of 3.7, the fitting procedure is less accurate. The shape of the experimental curve is indeed composed of a bell portion with a maximum amplitude of 0.2 and of a sharper zone peaking at 0.35. The model is obviously not able to capture this particular shape. The fitting of the experiments of Feng (1968), for $Sc = 7.1$ and 8.9 is better. These Sc correspond to more common values for practical wind engineering applications.

Table 2 presents the numerical values for dimensionless groups D_0, D_1, ξ_0 of VIV applications corresponding to Fig. 9. D_0 ranges from 1 to 11 when Sc decreases for the three geometries. D_1 ranges from 3 to 30 for the 4:1 rectangle and circular cylinders when Sc decreases, while it goes until 60 for the square cylinder. The pairs of values D_0, D_1 of Table 2 fall well in the region (3) of Fig. 3 (red dots). When Sc increases, ξ_0 decreases, while D_0 increases. Their values verify the condition $2\xi_0 D_0 > 1$ necessary to have $R_y \sim \xi_0^{-3/2}$, which was assumed to develop option 2.

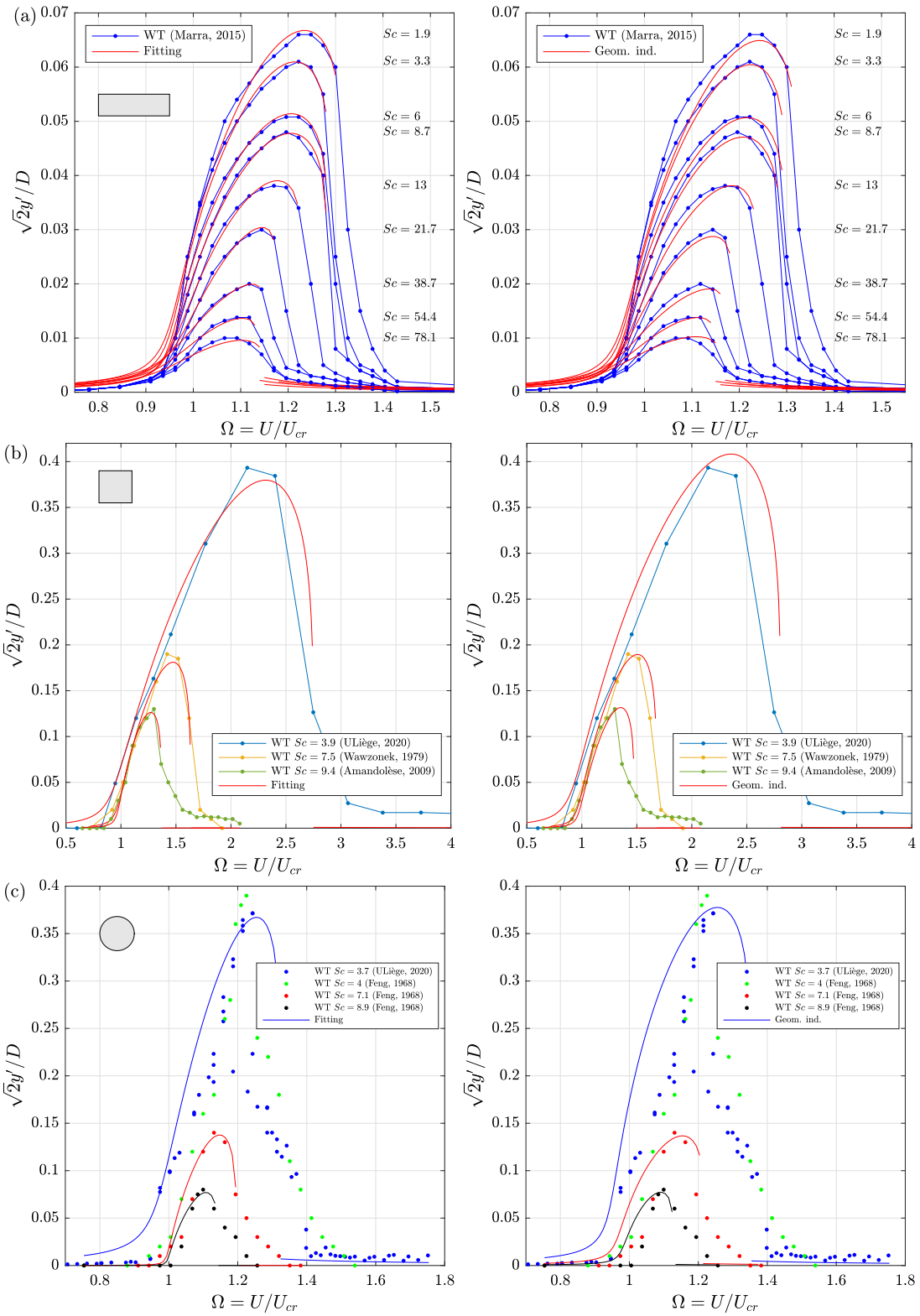

Fig. 9. Cylinder amplitude vs velocity ratio: comparison of WT data with fitting procedures for (a) 4:1 rectangle, (b) square and (c) circular cylinders. Left: least-square fitting (option 1); right: geometric indicators (option 2). (For interpretation of the references to colour in this figure legend, the reader is referred to the web version of this article.)

Table 2
Parameter identification results: comparison between fitting options.

Section shape	Sc	D_0		D_1		ξ_0		$2\xi_0 D_0$	
		Fit	Geom. ind.	Fit	Geom. ind.	Fit	Geom. ind.	Fit	Geom. ind.
4:1 Rectangle	1.9	10.3	9.8	29.9	28.7	0.12	0.14	2.47	2.74
"	3.3	9.7	9.3	27.6	28	0.15	0.18	2.91	3.35
"	6	7.3	8.7	24.5	24.9	0.21	0.24	3.07	4.18
"	8.7	6.5	6.8	22.7	23.2	0.25	0.27	3.25	3.67
"	13	4.9	5.5	19.1	19.3	0.33	0.3	3.23	3.3
"	21.7	3.4	3.8	12.2	12.7	0.4	0.42	2.72	3.19
"	38.7	2.8	3.2	6.2	7.3	0.52	0.55	2.91	3.52
"	54.4	1.7	2.1	4.5	6.7	0.67	0.61	2.28	2.56
"	78.1	1.1	1.5	3.7	6.1	0.72	0.57	1.58	1.71
Square	3.9	4.6	5	95	102	0.16	0.18	1.47	1.8
"	7.5	2.4	2.8	62	65	0.44	0.36	2.11	2.02
"	9.4	1.8	1.6	29	36	0.5	0.42	1.8	1.34
Circular	3.7	11	14	33	35	0.29	0.31	6.38	8.68
"	7.1	8	9	22	25	0.39	0.43	6.24	7.74
"	8.9	6	7	19	21	0.54	0.62	6.48	8.68

Results showed that the maximum amplitude of VIV curves happens for higher Ω when Sc decreases. It is a consequence of the synchronization mechanism: as discussed in Fig. 1, $\cot\psi = 0\,(\psi = \pi/2)$ for $\delta = D_1$ which corresponds to $\Omega \geq 1$. The parameters in D_1 justify this mistuning to the right according to the physical arguments of Tamura's model development (Tamura, 1981).

7. Discussion

In the asymptotic developments, some simplifications were made and justified. This led to rather simple analytic expressions for the phase (cubic algebraic equation), wake and displacement envelopes. These simplifications and the robustness of the developed asymptotic analysis explains the equivalence of results of options 1 and 2. This shows that there is no need to measure a very detailed VIV curve and procedure based on the abacus, can be sufficient as long as the geometric indicators can be accurately measured.

Fig. 10 shows an example of prediction for the case of the 4/1 rectangle. The model parameters D_0 and D_1 are obtained from the VIV curve corresponding to $Sc = 3.3$ only. The resulting model is then used to compute the VIV response for the other Sc (and ξ_s), i.e. by adapting the dimensionless groups with the varying damping ratios ξ_s or (ξ_0). It appears that the prediction approximates correctly the VIV curve for $Sc = 1.9$ but tends to be less accurate for higher Sc (8.7–13). This also translates the fact that the model parameters could be Scruton dependent.

The most challenging parameter in Tamura's model is f, which cannot be directly measured in WT (neither with static nor oscillating cylinder experiments). The added value of the present study is the identification of wake-oscillator model parameters. This parameter f is obtained from the parameter identification procedure after fitting (option 1) or geometric indicators (option 2) use. From the identified total damping ξ, the structural damping ratio ξ_s is subtracted to get the aerodynamic damping ξ_a, then f using the definition of ξ_a. Fig. 11 compares the f values of Tamura's prediction and the identification from the fitting (option 1) and geometric indicators (option 2) procedures. As expected, f depends on geometries but also on Sc (especially at low Sc). The identified f for the 4:1 rectangle and circular cylinder is close to the prediction of Tamura ($f = 1.16$ made for the circular cylinder only). Nevertheless, the identified value of f for the square cylinder is three times higher. Even higher values of f where used by Mannini et al. (2017) by modifying the size of the wake lamina. Rather than an adaptation of the wake geometry, in the present study, identified value of f comes from the data itself, not from a theoretical adaptation of the original model. This evolution of f with Sc can explain the results of Fig. 10. Indeed, the general shape of the VIV curve is asymmetric to the right but tends to symmetric around a $\Omega > 1$ when Sc increases (4:1 rectangle). The option 2 needs a VIV curve with a hysteresis and Tamura's model virtually accommodates with this hysteresis to obtain a VIV curve not centred on $\Omega = 1$. The aerodynamic damping in Tamura's model is based on the average C_D measured on a fixed cylinder but as f relies on quasi-steady theory, C_{Fy} could be used (force projected perpendicularly to the flow).

8. Conclusion

In this paper, an asymptotic analysis of the Tamura's wake-oscillator model was presented, leading to its averaged version. This developed analysis allows to transform the fast dynamics of the complete differential system to a slow dynamics model for the phase and response envelopes. The algebraic model has the advantage to be simple and is able to explain many features of the original model. The phase between the structural motion and wake variable plays a major role in the dynamics and the displacement envelope is deduced from it. Even if the model is simplified and seems decoupled, the response is the result of the interaction of the structure and the wake through the phase Eq. (8). The slow

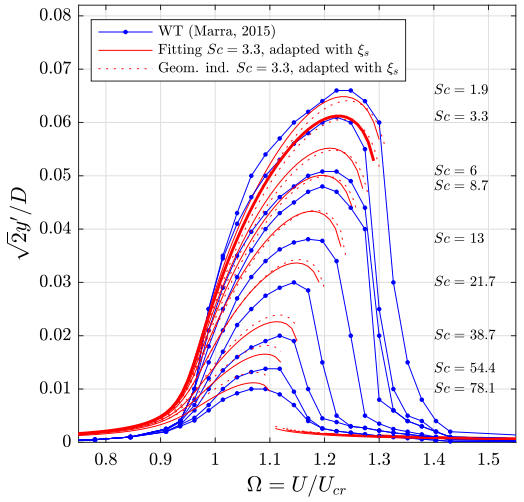

Fig. 10. Amplitude vs wind velocity ratio of a 4:1 rectangle: WT data (Marra et al., 2015), re-use of parameters from $Sc = 3.3$ fitting and adaptation with ξ_s.

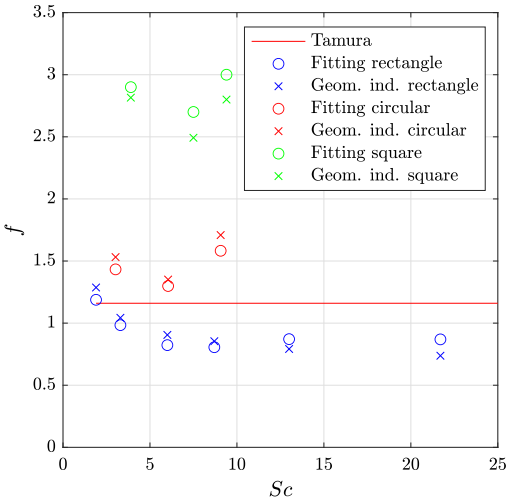

Fig. 11. Comparison of Tamura prediction of f and model parameter identification for different Sc and shapes from fitting options.

dynamics of the phase is governed by the dimensionless groups D_0, D_1. These two groups combine several parameters of Tamura's model which drive the VIV phenomenon. Both groups are positive and the corresponding VIV curve is hence asymmetric to the right, with hysteresis that depends on the combination of D_0 and D_1. For typical VIV applications, pairs of D_0, D_1 correspond to a VIV curve shape with a hysteresis to the right, see Fig. 3. This simple model allows to easily fit parameters to some WT data (amplitude vs wind velocity). Two options of a method aiming at fitting this simple closed-form expression to WT data are developed: (i) a least-square fitting and (ii) a fit with geometric indicators (height, width and asymmetry). Applications of these methods on WT data for 4:1 rectangle, square and circular cylinders showed accurate and equivalent results. The derivation of model parameters such as f from the identification procedure showed a dependency on geometry and Sc. This work opens several perspectives. Among others, it offers a simple and robust way to identify the VIV parameters (such as D_0, D_1, ξ_0) for non-axisymmetric cross-sections as a function of wind incidence or Reynolds number using other experimental data (WT, *in situ*). Also, the developments were made for the Tamura's model but can be extended to other VIV models from the literature with adapted developments.

CRediT authorship contribution statement

François Rigo: Conceptualization, Methodology, Software, Data curation, Writing, Visualization, Investigation, Validation. **Thomas Andrianne:** Conceptualization, Methodology, Writing, Visualization, Supervision, Validation, Reviewing and editing. **Vincent Denoël:** Conceptualization, Methodology, Writing, Visualization, Supervision, Validation, Reviewing and Editing.

Declaration of competing interest

The authors declare that they have no known competing financial interests or personal relationships that could have appeared to influence the work reported in this paper.

Acknowledgement

The authors want to thank the Belgian National Fund for Scientific Research (FNRS) for their support.

Appendix

The appendix gathers the solutions of the asymptotic analysis and Equations in Section 4.2, an alternative parameter identification for the width of the VIV curve and a presentation of the setup developed in this study.

A.1. Asymptotic analysis and geometric indicators equations solutions

Secularity conditions of Section 2.2 give three first order differential equations

$$R_y' = M_0 R_\alpha \sin\psi - \xi_0 R_y \tag{A.1}$$

$$R_\alpha' = A_0 R_y \sin\psi + A_1 R_y \cos\psi - \frac{R_\alpha^3}{8} + \frac{R_\alpha}{2} \tag{A.2}$$

$$\psi' = \left(A_0 \frac{R_y}{R_\alpha} + M_0 \frac{R_\alpha}{R_y}\right)\cos\psi - A_1 \frac{R_y}{R_\alpha}\sin\psi + \xi_0\delta. \tag{A.3}$$

Solutions of Eq. (15) are

$$c = \frac{\sqrt[3]{c_1/2}}{3} - \frac{\sqrt[3]{2}\left(-9a^2 + 12b + 3\right)}{3\sqrt[3]{c_1}} - a$$

$$c = -\frac{1 \pm i\sqrt{3}}{6\sqrt[3]{c_1/2}} - + \frac{(1 + \mp i\sqrt{3})\left(-9a^2 + 12b + 3\right)}{3\sqrt[3]{4c_1}} - a$$

where, $c_1 = -54a^3 + \sqrt{\left(-54a^3 + 108ab + 54a\right)^2 + 4\left(-9a^2 + 12b + 3\right)^3} + 108ab + 54a$, $a = \xi_0 D_0$ and $b = \xi_0 D_1$.

Solutions of Eq. (16) are

$$c = \pm\frac{1}{2}\sqrt{c_3} \pm \frac{1}{2}\sqrt{-c_3 + 2D_0 - 4 + \frac{4D_1}{c_3}}$$

where,

$c_3 = \frac{\sqrt[3]{2}(D_0+4)^2}{3c_2} + \frac{1}{3\sqrt[3]{2}}c_2 + \frac{2D_0-4}{3}$,

$c_2 = \sqrt[6]{c_1^2 - 4(D_0+4)^6 + c - 1}$

$c_1 = 2(2 - D_0)^3 - 72(D_0 + 1)(2 - D_0) + 108D_1^2$.

A.2. Present wind tunnel setup

The wind tunnel set-up developed in the present study consists in a smooth circular cylinder suspended vertically and free to oscillate horizontally (Fig. A.12a). This PVC cylinder has an external diameter of $D = 10$ cm, a thickness $e = 3$ mm and a length $L = 1440$ mm. It is supported by extension springs connected to a rigid frame attached to the ceiling and the ground of the test section of the Wind Tunnel Laboratory of University of Liège. The bending stiffness in the horizontal direction is equal to 6155 N/m, elastomers are added and a wind-off analysis showed a natural frequency of $f_0 = 7.8$ Hz and a damping ratio of $\xi = 0.1\%$. The velocity is measured with a Pitot tube (1), the cylinder horizontal displacement is measured with a laser (2) and a wireless accelerometer measures the horizontal acceleration (3). The flow velocity in the wake of the model (cobra probe (5)) is measured synchronously with the cylinder displacement (laser (2)) . The second set-up used in the present study is illustrated in Fig. A.12b, with a similar instrumentation and arrangement as Fig. A.12a but horizontally suspended and a square section ($D = 5$ cm).

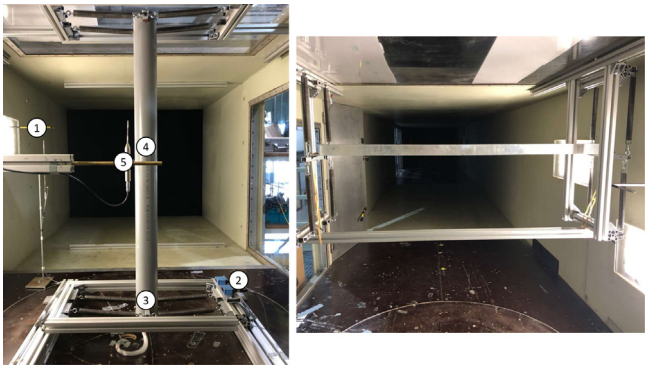

Fig. A.12. Frontal view of the WT set-up with sensors label for (a) circular and (b) square cylinders.

References

Amandolèse, X., Hémon, P., 2010. Vortex-induced vibration of a square cylinder in wind tunnel. C. R. Méc. 338 (1), 12–17.

Blevins, R.D., 1990. Flow-Induced Vibration. Van Nostrand Reinhold.

Brika, D., Laneville, A., 1993. Vortex-induced vibrations of a long flexible circular cylinder. J. Fluid Mech. 250, 481–508.

Chen, S.S., Zhu, S., Cai, Y., 1995. An unsteady flow theory for vortex-induced vibration. J. Sound Vib. 184 (1), 73–92.

Denoël, V., 2020. Derivation of a slow phase model of vortex-induced vibrations for smooth and turbulent oncoming flows. J. Fluids Struct. 99, 103145.

Facchinetti, M., de Langre, E., Biolley, F., 2004. Coupling of structure and wake oscillators in vortex-induced vibrations. J. Fluids Struct. 19, 123–140.

Farshidianfar, A., Zanganeh, H., 2010. A modified wake oscillator model for vortex-induced vibration of circular cylinders for a wide range of mass-damping ratio. J. Fluids Struct. 26 (3), 430–441.

Feng, C., 1968. The measurement of vortex induced effects in flow past stationary and oscillating circular and D-section cylinders. (Ph.D. thesis). In: Retrospective Theses and Dissertations, 1919-2007, University of British Columbia.

Gabbai, R.D., Benaroya, H., 2005. An overview of modeling and experiments of vortex-induced vibration of circular cylinders. J. Sound Vib. 282, 575–616.

Glendinning, P., 1994. Stability, Instability and Chaos: An Introduction to the Theory of Nonlinear Differential Equations. In: Cambridge Texts in Applied Mathematics, Cambridge University Press.

Golubitsky, M., Stewart, I., Schaeffer, D.G., 1989. Singularities and groups in bifurcation theory. Volume II. SIAM Rev. 31 (4), 703–704.

Hartlen, R.T., Currie, I.G., 1970. Lift-oscillator model of vortex-induced vibration. J. Eng. Mech. Div. 96, 577–591.

Hinch, E.J., 1991. Perturbation Methods. In: Cambridge Texts in Applied Mathematics, Cambridge University Press.

Krenk, S., Nielsen, S.R.K., 1999. Energy balanced double oscillator model for vortex-induced vibrations. J. Eng. Mech. 125, 263–235.

Labraga, L., Kahissim, G., Keirsbulck, L., Beaubert, F., 2007. An experimental investigation of the separation points on a circular rotating cylinder in cross flow. J. Fluids Eng. 129.

Larsen, A., 1995. A generalized model for assessment of vortex-induced vibrations of flexible structures. J. Wind Eng. Ind. Aerodyn. 57 (2), 281–294, Proceedings of the First IAWE European and African Regional Conference.

Lienhard, J.H., 1966. Synopsis of Lift, Drag, and Vortex Frequency Data for Rigid Circular Cylinders. In: Bulletin Washington State University. College of Engineering. Research Division, 300, Technical Extension Service, Pullman, Wash.

Lupi, F., Niemann, H.J., Höffer, R., 2018. Aerodynamic damping model in vortex-induced vibrations for wind engineering applications. J. Wind Eng. Ind. Aerodyn. 174, 281–295.

Mannini, C., 2020. Asymptotic analysis of a dynamical system for vortex-induced vibration and galloping. In: Lacarbonara, W., Balachandran, B., Ma, J., Tenreiro Machado, J.A., Stepan, G. (Eds.), Nonlinear Dynamics of Structures, Systems and Devices. Springer International Publishing, Cham, pp. 389–397.

Mannini, C., Massai, T., Marra, A.M., Bartoli, G., 2017. Interference of vortex-induced vibration and galloping: Experiments and mathematical modelling. Procedia Eng. 199, 3133–3138, X Int. Conf. on Structural Dynamics, EURODYN 2017.

Marra, A.M., Mannini, C., Bartoli, G., 2011. Van der Pol-type equation for modeling vortex-induced oscillations of bridge decks. J. Wind Eng. Ind. Aerodyn. 99 (6), 776–785, The Eleventh Italian National Conference on Wind Engineering, IN-VENTO-2010, Spoleto, Italy, June 30th - July 3rd 2010.

Marra, A.M., Mannini, C., Bartoli, G., 2015. Measurements and improved model of vortex-induced vibration for an elongated rectangular cylinder. J. Wind Eng. Ind. Aerodyn. 147, 358–367.

Matlab, 2019. Version 9.7.0 (R2019b). The MathWorks Inc., Natick, Massachusetts.

Païdoussis, M.P., Price, S.J., de Langre, E., 2010. Fluid-Structure Interactions: Cross-Flow-Induced Instabilities. Cambridge University Press.

Pikovsky, A., Kurths, J., Rosenblum, M., Kurths, J., 2003. Synchronization: A Universal Concept in Nonlinear Sciences. In: Cambridge Nonlinear Science Series, Cambridge University Press.

Scruton, C., 1981. An Introduction to Wind Effects on Structures. In: Engineering design guides, Design Council, the British Standards Institution and the Council of Engineering Institutions.

Simiu, E., Scanlan, R.H., 1996. Winds Effects on Structures: Fundamentals and Applications to Design. In: A Wiley-Interscience publication, Wiley.

Tamura, Y., 1981. Wake-oscillator model of vortex-induced oscillation of circular cylinder. J. Wind Eng. 1981 (10), 13–24.

Varty, R.L., Currie, I.G., 1984. Measurements near a laminar separation point. J. Fluid Mech. 138, 1–19.

Wawzonek, M.A., 1979. Aeroelastic behavior of square section prisms in uniform flow. (Ph.D. thesis). In: Retrospective Theses and Dissertations, 1919-2007, University of British Columbia.

Williamson, C.H.K., Roshko, A., 1988. Vortex formation in the wake of an oscillating cylinder. J. Fluids Struct. 2 (4), 355–381.